HAL
open science

Structure and Rheology in Vertex Models under Cell-Shape-Dependent Active Stresses

Shao-Zhen Lin, Matthias Merkel, Jean-François Rupprecht

To cite this version:

Shao-Zhen Lin, Matthias Merkel, Jean-François Rupprecht. Structure and Rheology in Vertex Models under Cell-Shape-Dependent Active Stresses. Physical Review Letters, 2023, 130 (5), pp.058202. 10.1103/PhysRevLett.130.058202 . hal-04049497

HAL Id: hal-04049497

https://hal.science/hal-04049497v1

Submitted on 28 Mar 2023

HAL is a multi-disciplinary open access archive for the deposit and dissemination of scientific research documents, whether they are published or not. The documents may come from teaching and research institutions in France or abroad, or from public or private research centers.

L'archive ouverte pluridisciplinaire **HAL**, est destinée au dépôt et à la diffusion de documents scientifiques de niveau recherche, publiés ou non, émanant des établissements d'enseignement et de recherche français ou étrangers, des laboratoires publics ou privés.

Structure and rheology in vertex models under cell shape-dependent active stresses

Shao-Zhen Lin,[1] Matthias Merkel,[1] and Jean-François Rupprecht[1,*]

[1] *Aix Marseille Univ, Université de Toulon, CNRS, CPT (UMR 7332), Turing Centre for Living systems, Marseille, France.*

(Dated: March 28, 2023)

Biological cells can actively tune their intracellular architecture according to their overall shape. Here we explore the rheological implication of such coupling in a minimal model of a dense cellular material where each cell exerts an active mechanical stress along its axis of elongation. Increasing the active stress amplitude leads to several transitions. An initially hexagonal crystal motif is first destabilized into a solid with anisotropic cells whose shear modulus eventually vanishes at a first critical activity. Increasing activity beyond this first critical value, we find a re-entrant transition to a regime with finite hexatic order and finite shear modulus, in which cells arrange according to a rhombile pattern with periodically arranged rosette structures. The shear modulus vanishes again at a third threshold beyond which spontaneous tissue flows and topological defects of the nematic cell shape field arise. Flow and stress fields around the defects agree with active nematic theory, with either contractile or extensile signs, as also observed in several epithelial tissue experiments.

Connecting the single-cell behavior to large-scale mechanical properties of biological tissues is key to understand development, regeneration, and disease [1]. Growing experimental evidence supports the idea that biological cells actively tune their intracellular architecture according to their overall shape. For instance, actomyosin [2–5] and microtubules (whether in *Drosophila* [6, 7] or in plants [5, 8]) tend to align along the direction of cell shape elongation. Such oriented fibers are known to generate anisotropic stress [9]. For instance, during *Drosophila* germ band extension, cells involved in rosette formation exhibit actin polymerization at opposite corners [10], which effectively creates an extensile active stress, Fig. 1a.

Here, we explore the consequences of such cell-shape feedback for the tissue-scale behavior. We study a minimal model where a bulk cellular active stress $\boldsymbol{\sigma}^{(\mathrm{act})}$ is created by filaments which in turn align with cell shape, represented by a tensor $\boldsymbol{Q}$ (Fig. 1b-d). To lowest order,

$$\boldsymbol{\sigma}^{(\mathrm{act})} = -\beta \boldsymbol{Q}, \tag{1}$$

which we incorporate in a computational model for dense epithelial tissue. For $\beta > 0$ (resp. $\beta < 0$), cells actively push (resp. pull) on their neighbours along their direction of elongation [11, 12].

Relations like Eq. (1) have been considered in tissue models before. For instance, in active hydrodynamic theories, where both $\boldsymbol{\sigma}^{(\mathrm{act})}$ and $\boldsymbol{Q}$ are defined by averages over several cells, Eq. (1) gives rise to a classical flow instability [13–15]. In the absence of confining boundaries, this instability occurs at arbitrarily small activities $\beta > 0$. An active stress as in Eq. (1) has also been included in cell-based phase field simulations [16]. In these simulations, the transition to spontaneous flows occurs for a critical value of β which (i) is finite and appears to be independent of the system size, contrasting with active hydrodynamic theory results, and (ii) scales linearly with a cell surface tension. So far, while Ref. [16] provided an intuitive conjecture, a precise understanding of both is missing. Is a finite activity threshold a general property of deformable cellular materials?

We address these questions by combining analytical arguments and vertex model simulations. Vertex models describe epithelial tissues as polygonal tilings [17–19]. Forces on the polygon vertices are defined by a mechanical energy: $E = 1/2 \sum_J [K_A(A_J - A_0)^2 + K_P(P_J - P_0)^2]$ where the sum is over all cells J of the tissue, and A_J and P_J are cell area and perimeter, respectively. The parameters A_0 and P_0 are preferred cell area and perimeter with the associated rigidities K_A and K_P, respectively. A transition occurs at $P_0 = P_0^*$, with the tissue behaving as a yield stress solid for $P_0 < P_0^*$ and as a fluid for $P_0 \geq P_0^*$ [20, 21]. The numerical value of P_0^* is in the range $3.72 \ldots 3.94$, with a value that depends on the disorder in the cellular packing [20–24] (SM [25], Sec. I). This solid-to-fluid transition can additionally be driven by cell-based active polar forces [26–28], or by active tension fluctuations at cell–cell junctions [29], or by a chemomechanical feedback loop between tension and myosin ac-

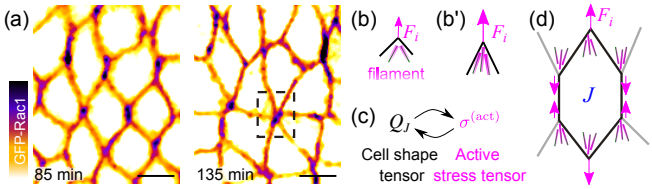

FIG. 1. (a) Experimental images of the basal side of *Drosophila* epithelial cells during germ band extension with marked GFP-Rac1 marking filament growth activity; six-fold vertex indicated by a square. Scale bar: 5 μm. Experimental images provided by Y. Toyama. (b) A model of increasingly strong filament growth (magenta rods) for increasingly acute cell corners (black wedge). (c) Our model where active stresses are defined by cell shape. (d) Active forces in a cell (index J) of our vertex model, mimicking the effect of growing filaments at wedge-like cell corners.

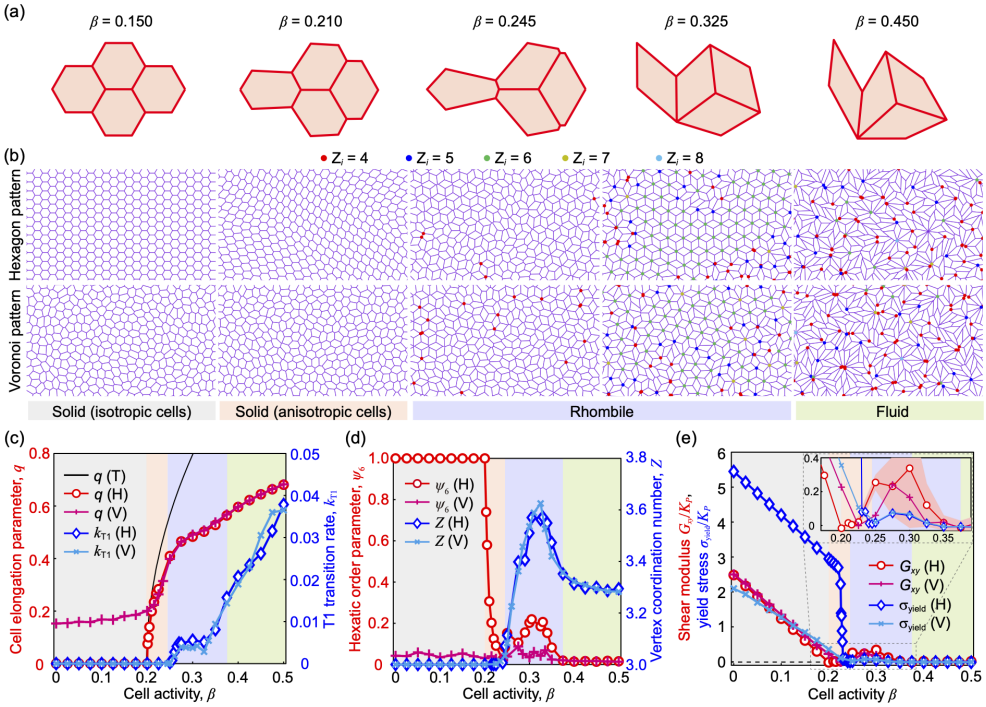

FIG. 2. (a, b) Morphology of (a) a four-cell system and (b) a cell sheet at different activities β, with an initially hexagon (top) or Voronoi pattern (bottom). In (b), we mark vertices with coordination number $Z_i > 3$. (c) Cell elongation parameter q, and T1 transition rate k_{T1} versus cell activity β, for an initially hexagonal (H) or Voronoi (V) pattern. The solid black line refers to an analytical approximation of q. (d) Hexatic order parameter ψ_6 and average vertex coordination number Z versus cell activity β. (e) Long-time shear modulus G_{xy} and yield stress σ_{yield} versus cell activity β. Inset: red shaded area indicates the mean $\pm$ standard deviation of the shear modulus for the initially hexagonal pattern, estimated from $n = 5$ simulations. Default parameter values with $P_0 = 1$.

tivity along cell–cell junctions [30, 31]. The vertex model solid-to-fluid transition is also echoed in experiments on biological tissues [32].

Here we introduce Eq. (1) in the vertex model framework, and depending on the value of P_0, we find different kinds of transitions. For $P_0 < P_0^*$, we find four different regimes upon increasing β (Fig. 3). For $\beta < \beta_1$ the tissue is solid with isotropic cells. For $\beta_1 < \beta < \beta_2$, cell shapes are anisotropic. For $\beta_2 < \beta < \beta_3$, we find a regime with rhombile cells, many-fold vertices, long-range crystalline order and finite shear modulus. Finally, at $\beta_3 < \beta$, the tissue turns into an active fluid and displays constant flows that lack large-scale coherence. Conversely, for $P_0 \geq P_0^*$, we find that a solid regime with anisotropic cells for $\beta \leq 0$ directly transitions to the active fluid regime for $\beta > 0$. We demonstrate why a finite activity threshold β_3 appears in the solid regime, $P_0 < P_0^*$, in our cell-based model; to overcome the yield stress in the solid phase, a finite $\beta = \beta_3$ is required for active flows to appear, as in Ref. [16]. Meanwhile, active hydrodynamic theories as in [13, 14] describe tissues as fluids, which corresponds in our model to $P_0 \geq P_0^*$. In this case, active flows can appear without threshold, i.e. $\beta_3 = 0$.

Method We implement Eq. (1) through the following friction-based dynamics for the vertex positions $\boldsymbol{r}_i$

$$\gamma \frac{\mathrm{d}\boldsymbol{r}_i}{\mathrm{d}t} = \boldsymbol{F}_i^{(\mathrm{svm})} + \boldsymbol{F}_i^{(\mathrm{act})}. \tag{2}$$

Here, γ is a friction coefficient, $\boldsymbol{F}_i^{(\mathrm{svm})} = -\partial E/\partial \boldsymbol{r}_i$ are the standard vertex model (svm) forces, and $\boldsymbol{F}_i^{(\mathrm{act})}$ are the active forces induced by the active anisotropic bulk stresses $\boldsymbol{\sigma}^{(\mathrm{act})}$ defined for each cell according to Eq. (1). There are different ways to translate the cellular bulk stresses $\boldsymbol{\sigma}^{(\mathrm{act})}$ into the vertex forces $\boldsymbol{F}_i^{(\mathrm{act})}$ [33–36]. Here we use the approach proposed by Tlili et al. [33, 34, 36], which relies on Cauchy's stress definition. For the cell shape anisotropy tensor $\boldsymbol{Q}_J$ in Eq. (1), we use the symmetric, traceless tensor

$$\boldsymbol{Q}_J = \frac{1}{P_J} \sum_k l_k \boldsymbol{t}_k \otimes \boldsymbol{t}_k - \frac{\boldsymbol{I}}{2}, \tag{3}$$

where P_J is the cell perimeter; the sum is over all sides k of the cell J, and l_k and $\boldsymbol{t}_k$ denote length and unit tangent vector of side k, respectively. The eigenvalues and principal directions of $\boldsymbol{Q}_J$ provide metrics for the cell shape and cell orientation. We measure the cell shape anisotropy by $q_J = \sqrt{2\mathrm{tr}(\boldsymbol{Q}_J^2)} \in [0, 1)$, with $q_J = 0$ for round cells and $q_J \to 1$ for increasingly elongated ones.

We initialize the system with cells arranged according to either (i) a regular hexagonal pattern with small random deviations in the vertex positions, or (ii) random Voronoi tessellations (SM [25], Sec. I). In addition, we perform cell-neighbor exchanges (T1 transitions) for cell–cell interfaces shorter than a length threshold Δ_{T1} (SM [25], Sec. I). We use periodic boundary conditions with fixed system size. We set $K_A = 1$, $A_0 = 1$, $K_P = 0.02$, $\gamma = 1$, $P_0 = 1$, $\Delta_{\mathrm{T1}} = 0.01$, and $N = 10^3$ cells if not otherwise stated (SM [25], Sec. I; Table S1).

Results Increasing β, we observe several rheological and structural transitions (Fig. 2a,b; Movies S1-S3). In Fig. 3 we show the dependence of these transitions on both β and P_0; however, in the following, we focus on the case $P_0 = 1$ (Fig. 2). For small $\beta < \beta_1 \approx 0.20$ the vertex model tissue is solid (Fig. 2e) with isotropic

cell shapes (Fig. 2c), where the average cell elongation is $q = 0$ (resp. $q \approx 0.16$) when using a hexagonal (resp. Voronoi) initial state. When β increases beyond β_1, cell shapes become anisotropic, as indicated by an increase in q (Fig. 2c). This is accompanied by a decrease in the hexatic order parameter ψ_6 (Fig. 2d), defined as $\psi_6 = |\sum \Psi_j/N|$, where $\Psi_j = \sum_{k\in\text{neighbors}} \exp(\mathrm{i}6\theta_{jk})/N_j$ and $\theta_{jk} = \arg(\boldsymbol{r}_k - \boldsymbol{r}_j)$ [37–39]. While in this regime the shear modulus vanishes for the hexagonal initial state, the tissue remains solid, as verified through the examination of the yield stress (Fig. 2e, SM [25], Sec. I). The transition point β_1 decreases with increasing P_0 up until the critical point P_0^* (Fig. 3).

The cell shape transition at $\beta = \beta_1$ occurs because the β term in Eq. (1) effectively corresponds to a negative shear modulus. As a consequence, when $\beta > \beta_1$, the total cellular shear modulus decreases to zero, destabilizing the isotropic cell shape. To see this, we start from the Batchelor stress of a vertex model cell with perimeter P and area A [36, 40–42], whose anisotropic part $\tilde{\boldsymbol{\sigma}}$ is (SM [25], Sec. I):

$$\tilde{\boldsymbol{\sigma}} = \left[\frac{K_P P(P-P_0)}{A} - \beta\right]\boldsymbol{Q}. \tag{4}$$

To obtain the global tissue shear modulus G_{aff} in an analytical mean-field picture, we apply an affine pure shear strain ϵ to an isotropic cell, which creates the cell shape anisotropy $q = 3\epsilon/2$ to lowest order in ϵ (SM [25], Sec. II). Comparing Eq. (4) to $\tilde{\sigma} = 2G_{\text{aff}}\epsilon$, we obtain:

$$G_{\text{aff}} = \frac{3}{8}\Big[K_P P(P-P_0) - \beta\Big]. \tag{5}$$

Here, we have used $A \approx A_0 = 1$, which corresponds to the limit of incompressible cells. Testing Eq. (5) numerically, where we also include all non-affinities, we find the same result, except for a prefactor: $G_{\text{non-aff}} \approx 2G_{\text{aff}}/3$. To determine the value of the perimeter P appearing in Eq. (5), we use that in the isotropic solid regime $P = P_0^* \approx 3.722$ for a hexagonal tissue [21, 43]. Isotropic cell shape thus becomes unstable for $\beta > \beta_1(P_0)$ with (SM [25], Sec. II):

$$\beta_1(P_0) = K_P P_0^*(P_0^* - P_0). \tag{6}$$

This equation exactly predicts the stability of the regular hexagonal crystal (white lines in Fig. 3). This mean-field picture also explains how in the regime $P_0 < P_0^\star$ cells elongate for $\beta > \beta_1(P_0)$. For an affinely sheared isotropic cell, the perimeter increases quadratically with its shape anisotropy as $P = P_0^*(1 + q^2/3)$ (SM [25], Sec. II) [24]. Inserting this in Eq. (4) and combining it with $\tilde{\sigma} = (\partial E/\partial\epsilon)/2A$, we obtain an effective potential of the cell depending on its shape anisotropy $E_{\text{eff}}(q)$, which reads to fourth order in q (SM [25], Sec. II):

$$E_{\text{eff}}(q) = \frac{1}{3}\Big[\beta_1(P_0) - \beta\Big]q^2 + \frac{1}{18}K_P P_0^*\big(2P_0^* - P_0\big)q^4. \tag{7}$$

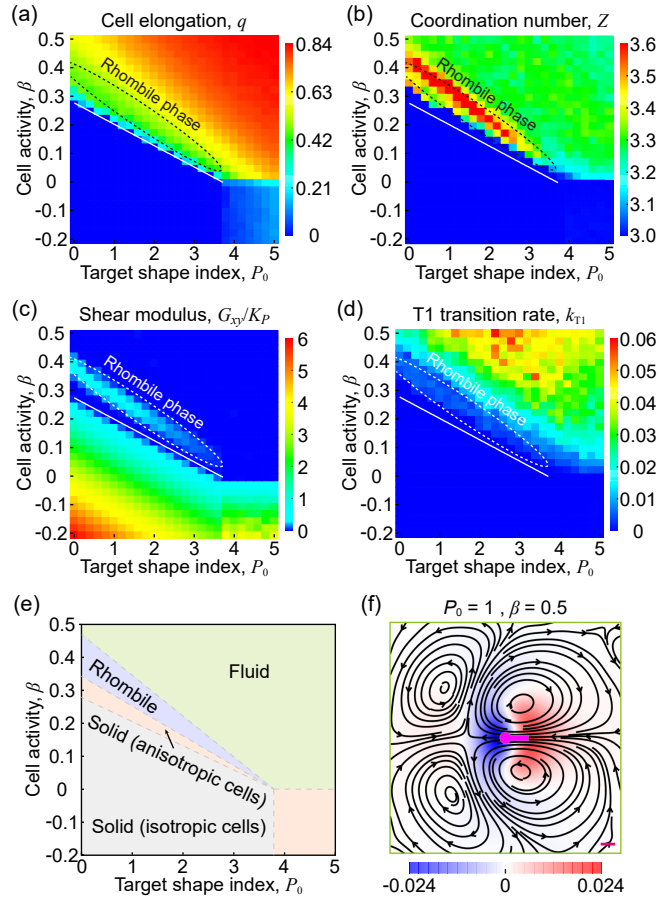

FIG. 3. Diagrams depending on the target shape index P_0 (inter-cellular tension) and cell bulk activity β, showing (a) average cell elongation parameter q, (b) average vertex coordination number Z, (c) shear modulus G_{xy}, and (d) T1 topological transition rate k_{T1}. Here, the solid white curves refer to the theoretical prediction $\beta_1(P_0)$, Eq. (6), for the transition between the solid regime with isotropic cells and the solid regime with anisotropic cells. (e) Overall phase diagram. (f) Average isotropic stress (color map) and velocity (black streamlines) fields near +1/2 defects, with $P_0 = 1$ and $\beta = 0.5$. Average over $n = 44368$ defects. Scale bar = 1 cell.

The energy minimum for $\beta < \beta_1$ is at $q_{\min} = 0$, while for $\beta > \beta_1$ the minimum is at $q_{\min}(\beta) = \sqrt{3(\beta-\beta_1)/K_P P_0^*(2P_0^* - P_0)}$, which corresponds to a typical pitchfork bifurcation. Indeed, this predicts well the observed cell elongation in the regime close to β_1 for $P < P_0^\star$ (Fig. 3c, SM [25], Sec. II).

The behavior of cell-shape elongation q is different in the regime $P_0 > P_0^\star$, where we observe a *discontinuous* increase in q and coordination number Z as soon as β is increased above zero (Fig. 3a,b, SM [25], Sec. VI). The discontinuity in q can be understood by first looking at a system with $\beta = 0$ and given cell elongation q. In this case, for $P_0 > P_0^\star$, the system is floppy with vanishing energy $E(q) = 0$ as long as $q < q_{\text{crit}}$, where the critical q value is $q_{\text{crit}} \sim \sqrt{P_0 - P_0^*}$. Beyond this value, cells

and the vertex model tissue start to attain a finite shear modulus [24]. As a consequence, as soon as β is set to a positive value, for $q < q_{\rm crit}$ the energy becomes $E(q) \sim -\beta q^2$, and so any state $q < q_{\rm crit}$ becomes unstable. Thus, for small positive β, cell elongation will make a jump from zero to a value close to $q_{\rm crit}$.

For $P_0 < P_0^*$, beyond $\beta > \beta_2$ (with $\beta_2 \approx 0.24$ for $P_0 = 1$), starts a regime marked by an increasing hexatic order ψ_6 (Fig. 2b-d). For tissues initiated in the near hexagonal pattern, this order appears to be even long-ranged (SM [25], Sec. I). We call this the *rhombile* regime, because domains appear where cells attain a rhombic shape, which arrange into a periodic arrangement of six-fold vertices (Fig. 2b). Correspondingly, the rhombile regime is marked by the increase in the average vertex coordination number Z (Fig. 2d).

The emergence of the rhombile pattern and manyfold vertices can be understood from single- and four-cell systems. Indeed, at a critical value of $\beta_2^{(1)} \approx 0.27$ for the single-cell system ($\beta_2^{(4)} \approx 0.25$ for the four-cell system), the two shortest edges of a hexagonal cell shrink to length zero, resulting in the observed rhombic cell shapes (Fig. 2a; Movie S4-S5; SM [25] Sec. II).

We find that the shear modulus in the rhombile regime is finite and peaks when the rhombile domain extension is maximal at around $\beta^* \approx 0.3$, which coincides with local maxima in the hexatic order ψ_6 and coordination number Z (Fig. 2d). We understand this by considering a single cell: at $\beta^* = 0.3$, the cell reaches a regular diamond shape with two $\pi/3$ and two $2\pi/3$ angles. This shape (also called *calisson* [44]) is the building block of the crystal rhombile pattern (SM [25], Fig. S11b). When $\beta < \beta^* = 0.3$ (resp. $\beta > \beta^* = 0.3$), acute angles above (resp. below) $\pi/3$ form in the single cell, leading to frustration in the rhombile domains, which can destabilize them.

However, despite a finite shear modulus, the rhombile regime exhibits a finite steady-state T1 transition rate (Fig. 2d; SM [25] Sec. III; Movie S2). This may appear paradoxical at first sight, since T1 transitions are expected to relax the applied stress [45], leading to a long-time fluid material response. Yet such argument may not hold for an active system at steady state, as considered here. Further, we notice that these T1 transitions are generated at the interfaces, rather than in the bulk, of the rhombile crystal domains (Movie S2).

The shear modulus eventually vanishes at $\beta_3 \approx 0.37$ for $P_0 = 1$. We find that this value matches the one at which the shear modulus of the perfect rhombile crystal vanishes (SM [25], Sec. III). This suggests that the finite shear modulus of the rhombile regime is caused by rhombile crystal domains.

For $\beta > \beta_3$, the system flows continuously, where the steady-state T1 transition rate increases with activity (Fig. 2e, 3d and Movie S2). Such flow already appears in a four-cell system for an intermediate activity range

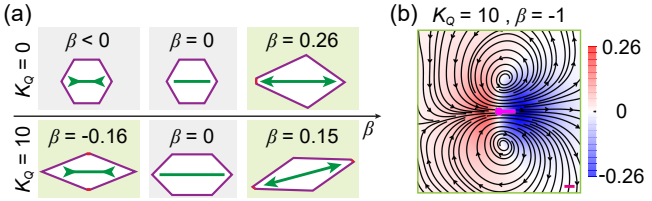

FIG. 4. Tissue flows and topological defects in the contractile regime ($\beta < 0$) in the presence of a passive cell elongation energy. (a) Sketch of cell activity leading to cell edge vanishing. Here, we mark the edges to vanish as red ones. Background color: gray for solid regime and light green for fluid regime. (b) Average isotropic stress (colorbar) and the velocity (streamlines) near $+1/2$ topological defects ($n = 25323$ defects. Scale bar = 1 cell), where $K_Q = 10$ and $\beta = -1$. Other parameters: $P_0 = 1$ and $q_0 = 0.8$.

(Movie S6). This flowing regime exhibits features of an active nematic material. For instance, coarse-graining of the cell orientation field reveals the presence of $\pm 1/2$ topological defects in the fluid regime (SM [25], Sec. V) [46, 47]. The stress and velocity patterns around $\pm 1/2$ topological defects are qualitatively consistent with those predicted in an incompressible material with extensile nematic activity [15, 16, 48] (Fig. 3f; SM [25], Sec. V). We note, however, the presence of a backward flow at the tip of $+1/2$ defects (Fig. 3f) that is reminiscent of *negative wake* reported in driven yield-strain materials [49]. A similar *negative wake* flow pattern is visible in experiments on Madin-Darby Canine Kidney cell monolayers [33, 50] (see SM [25], Sec. VIII).

Taken together, our results show that the existence of a yield stress explains the onset of active flows beyond a finite critical activity $\beta_3 > 0$, while active continuum models [13, 14], predict active flows at any finite activity, i.e. $\beta_3 = 0$. In our vertex model, such a difference arises as a function of P_0. For $P_0 < P_0^\star$, where the vertex model behaves as yield stress solid, we showed that β acts as a negative shear modulus, destabilizing the tissue beyond a critical value that increases with the distance to $P_0^\star$. In contrast, we observe that for the fluid vertex model regime, $P_0 > P_0^\star$, any positive β destabilizes the tissue, inducing a sharp increase in flow (Fig. 3d, SM [25], Sec. VI). Comparing both cases, we conclude that while any positive activity leads to flows in a fluid material, a yield stress creates a finite activity threshold to flow. This is likely the case in Ref. [16], because the employed phase field model essentially describes a foam that, expectedly, displays a yield stress.

In contrast to active hydrodynamic theory predictions [13, 15, 48], the cell-based model by Ref. [16] and the model we discussed so far do not exhibit spontaneous flows in the contractile regime ($\beta < 0$). One could take this as an indication that the observed transition to spontaneous flows is qualitatively different from the known instability of active hydrodynamic theory [13, 15, 48].

However, spontaneous flows can also exist in the contractile regime, $\beta < 0$. To show this, we included in our model the tendency of cells to attain a finite elongation q_J through an additional energy term, $E_{\rm el} = \sum_J K_Q[q_J^2 - q_0^2]^2/8$, where $K_Q \geq 0$ and q_0 refers to a preferred cell elongation parameter.

Using this model, we observe spontaneous tissue flows in both the extensile ($\beta > 0$) and the contractile regime ($\beta < 0$), with cells displaying rhombic shapes (Fig. 4a, Movie S7) and both the stress field and the flow field qualitatively agree with predictions of active hydrodynamic theories (Figs. 4(b); SM [25], Sec. VII) as well as experiments [11, 51–54].

Lastly, we tested how much our results depend on the definition of the $\boldsymbol{Q}$ tensor used in Eq. (1) (SM [25], Sec. IV). We find that the transitions in cell shape and rigidity are generic, but not the appearance of the rhombile crystal domains. In addition, we also tested the case of no perimeter elasticity ($K_P = 0$) but with a constant cell-cell interfacial tension instead [29]; we find the same results regarding the transition to flows and the onset of a rhombile phase (Fig. S23).

Conclusion We studied how a feedback of cell shape on the cellular active stress generation affects collective tissue dynamics. We show that increasing such a feedback eventually fluidifies the vertex model tissue, yet through a series of intermediate steps displaying hexatic order, enhanced finite shear modulus and spontaneous T1 transitions. We find that spontaneous flows can be thresholdless also for cellular materials and are not limited to the extensile regime.

Our prediction of *rhombile domains* could potentially also explain why, during the *Drosophila* germ band extension process [10], cells display rhombic shapes before the onset of six-fold vertices, Fig. 1a. These cell shape changes are shown to be triggered by actin protrusions [10]. At early stages, these protrusions are located at opposite ends of the cell, suggesting that the resulting set of forces could be compatible with the one considered in our extensile active stress model, Fig. 1.

Perspectives While in most instances active cellular materials have been studied in the vertex model through the introduction of traction forces against a resting substrate [28, 55], here we introduce activity through momentum-conserving forces $\boldsymbol{F}_i^{(\rm act)}$ [36]. Implementing this kind of activity within a Galilean invariant dissipation framework [42] could be useful to describe tissue flows in conditions of low environmental friction e.g. free-standing tissues, pre-implantation embryos or intestinal organoids [56].

Acknowledgements We thank the Centre Interdisciplinaire de Nanoscience de Marseille (CINaM) and the Laboratoire Adhésion Inflammation (LAI) for providing office space. J.F. R. and S-Z. L. thank F. Graner, T. Saunders and Y. Toyama for discussions and for the experimental data shown in Fig. 1, as well as B. Ladoux and R.-M. Mège for the experimental data shown in Fig. S22. The project leading to this publication has received funding from France 2030, the French Government program managed by the French National Research Agency (ANR-16-CONV-0001) and from Excellence Initiative of Aix-Marseille University - A*MIDEX. J.F. R. is also funded by ANR-20-CE30-0023 COVFEFE.

* jean-francois.rupprecht@univ-amu.fr

[1] B. Ladoux and R. M. Mège, Nature Reviews Molecular Cell Biology **18**, 743 (2017).
[2] A. Saraswathibhatla and J. Notbohm, Physical Review X **10**, 011016 (2020).
[3] M. Gupta, B. L. Doss, L. Kocgozlu, M. Pan, R. M. Mège, A. Callan-Jones, R. Voituriez, and B. Ladoux, Physical Review E **99**, 012412 (2019).
[4] L. Blanchoin, R. Boujemaa-Paterski, C. Sykes, and J. Plastino, Physiological Reviews **94**, 235 (2014).
[5] V. Gorelova, J. Sprakel, and D. Weijers, Nature Plants , 1 (2021).
[6] N. A. Dye, M. Popović, K. V. Iyer, J. F. Fuhrmann, R. Piscitello-Gómez, S. Eaton, and F. Jülicher, Elife **10**, e57964 (2021).
[7] A. Singh, T. Saha, I. Begemann, A. Ricker, H. Nüsse, O. Thorn-Seshold, J. Klingauf, M. Galic, and M. Matis, Nature Cell Biology **20**, 1126 (2018).
[8] V. Mirabet, P. Krupinski, O. Hamant, E. M. Meyerowitz, H. Jönsson, and A. Boudaoud, PLoS Computational Biology **14**, 1 (2018).
[9] J. Prost, F. Jülicher, and J. F. Joanny, Nature Physics **11**, 111 (2015).
[10] Z. Sun, C. Amourda, M. Shagirov, Y. Hara, T. E. Saunders, and Y. Toyama, Nature Cell Biology **19**, 375 (2017).
[11] G. Duclos, C. Blanch-Mercader, V. Yashunsky, G. Salbreux, J.-F. Joanny, J. Prost, and P. Silberzan, Nature Physics **14**, 728–732 (2018).
[12] T. B. Saw, A. Doostmohammadi, V. Nier, L. Kocgozlu, S. Thampi, Y. Toyama, P. Marcq, C. T. Lim, J. M. Yeomans, and B. Ladoux, Nature **544**, 212 (2017).
[13] R. A. Simha and S. Ramaswamy, Physical Review Letters **89**, 058101 (2002).
[14] R. Voituriez, J. F. Joanny, and J. Prost, Europhysics Letters **70**, 404 (2005).
[15] M. C. Marchetti, J. F. Joanny, S. Ramaswamy, T. B. Liverpool, J. Prost, M. Rao, and R. A. Simha, Review of Modern Physics **85**, 1143 (2013).
[16] R. Mueller, J. M. Yeomans, and A. Doostmohammadi, Physical Review Letters **122**, 048004 (2019).
[17] A. G. Fletcher, M. Osterfield, R. E. Baker, and S. Y. Shvartsman, Biophysical Journal **106**, 2291–2304 (2014).
[18] S. Alt, P. Ganguly, and G. Salbreux, Philosophical Transactions of the Royal Society B: Biological Sciences **372** (2017).
[19] E. Hannezo, J. Prost, and J.-F. Joanny, Proceedings of the National Academy of Sciences of the United States of America **111**, 27 (2014).
[20] R. Farhadifar, J. C. Röper, B. Aigouy, S. Eaton, and F. Jülicher, Current Biology **17**, 2095 (2007).
[21] D. Bi, J. H. Lopez, J. M. Schwarz, and M. L. Manning, Nature Physics **11**, 1074 (2015).
[22] D. M. Sussman and M. Merkel, Soft Matter **14**, 3397

(2018).
[23] M. Merkel, K. Baumgarten, B. P. Tighe, and M. L. Manning, Proceedings of the National Academy of Sciences of the United States of America **116**, 6560 (2019).
[24] X. Wang, M. Merkel, L. B. Sutter, G. Erdemci-Tandogan, M. L. Manning, and K. E. Kasza, Proceedings of the National Academy of Sciences of the United States of America **117**, 13541 (2020).
[25] The Supplemental Material at [URL] provides further details of analytical calculations and numerical simulations, which includes Refs. [57-59].
[26] D. L. Barton, S. Henkes, C. J. Weijer, and R. Sknepnek, PLOS Computational Biology **13**, 1 (2017).
[27] D. Bi, X. Yang, M. C. Marchetti, and M. L. Manning, Physical Review X **6**, 021011 (2016).
[28] S. Z. Lin, S. Ye, G. K. Xu, B. Li, and X. Q. Feng, Biophysical Journal **115**, 1826–1835 (2018).
[29] S. Kim, M. Pochitaloff, G. A. Stooke-Vaughan, and O. Campàs, Nature Physics **17**, 859–866 (2021).
[30] R. Sknepnek, I. Djafer-Cherif, M. Chuai, C. J. Weijer, and S. Henkes, arXiv , arXiv:2106.12394 (2022).
[31] F. Pérez-Verdugo and S. Banerjee, arXiv , arXiv:2211.05591 (2022).
[32] E. Hannezo and C.-P. Heisenberg, Trends in Cell Biology **0** (2022).
[33] S. Sonam, L. Balasubramaniam, S.-Z. Lin, Y. M. Y. Ivan, I. Pi-Jaumà, C. Jebane, M. Karnat, Y. Toyama, P. Marcq, J. Prost, R.-M. Mège, J.-F. Rupprecht, and B. Ladoux, Nature Physics (2022).
[34] S. Tlili, J. Yin, J.-F. Rupprecht, M. A. Mendieta-Serrano, G. Weissbart, N. Verma, X. Teng, Y. Toyama, J. Prost, and T. E. Saunders, Proceedings of the National Academy of Sciences of the United States of America **116**, 25430–25439 (2019).
[35] J. Comelles, S. Soumya, L. Lu, E. Le Maout, S. Anvitha, G. Salbreux, F. Jülicher, M. M. Inamdar, and D. Riveline, eLife **10** (2021).
[36] S. Z. Lin, M. Merkel, and J.-F. Rupprecht, The European Physical Journal E **45**, 1 (2022).
[37] Y. W. Li and M. P. Ciamarra, Physical Review Materials **2**, 045602 (2018).
[38] M. Paoluzzi, L. Angelani, G. Gosti, M. C. Marchetti, I. Pagonabarraga, and G. Ruocco, Physical Review E **104**, 044606 (2021).
[39] A. Pasupalak, L. Yan-Wei, R. Ni, and M. P. Ciamarra, Soft Matter **16**, 3914 (2020).
[40] G. K. Batchelor, Journal of Fluid Mechanics **41**, 545 (1970).
[41] A. W. C. Lau and T. C. Lubensky, Physical Review E **80**, 011917 (2009).
[42] A. Nestor-Bergmann, G. Goddard, S. Woolner, and O. E. Jensen, Mathematical Medicine and Biology **35**, 1 (2018).
[43] D. B. Staple, R. Farhadifar, J.-C. Röper, B. Aigouy, S. Eaton, and F. Jülicher, The European Physical Journal E **33**, 117 (2010).
[44] C. Alsina and R. Nelsen, *A Mathematical Space Odyssey* (2015).
[45] P. Marmottant, A. Mgharbel, J. Käfer, B. Audren, J. P. Rieu, J. C. Vial, B. V. D. Sanden, A. F. Marée, F. Graner, and H. Delanoë-Ayari, Proceedings of the National Academy of Sciences of the United States of America **106**, 17271 (2009).
[46] A. J. Vromans and L. Giomi, Soft Matter **12**, 6490 (2016).
[47] S. J. DeCamp, G. S. Redner, A. Baskaran, M. F. Hagan, and Z. Dogic, Nature Materials **14**, 1110 (2015).
[48] L. Giomi, Physical Review X **5**, 031003 (2015).
[49] I. Cheddadi, P. Saramito, B. Dollet, C. Raufaste, and F. Graner, European Physical Journal E **34** (2011).
[50] L. Balasubramaniam, A. Doostmohammadi, T. B. Saw, G. H. N. S. Narayana, R. Mueller, T. Dang, M. Thomas, S. Gupta, S. Sonam, A. S. Yap, *et al.*, Nature Materials **20**, 1156 (2021).
[51] G. Duclos, C. Erlenkämper, J.-F. Joanny, and P. Silberzan, Nature Physics **13**, 58–62 (2017).
[52] K. Kawaguchi, R. Kageyama, and M. Sano, Nature **545**, 327 (2017).
[53] C. Blanch-Mercader, V. Yashunsky, S. Garcia, G. Duclos, L. Giomi, and P. Silberzan, Physical Review Letters **120**, 208101 (2018).
[54] A. Doostmohammadi, J. Ignés-Mullol, J. M. Yeomans, and F. Sagués, Nature Communications **9**, 1 (2018).
[55] F. Giavazzi, M. Paoluzzi, M. Macchi, D. Bi, G. Scita, M. L. Manning, R. Cerbino, and M. C. Marchetti, Soft Matter **14**, 3471 (2018).
[56] N. Khalilgharibi, J. Fouchard, N. Asadipour, R. Barrientos, M. Duda, A. Bonfanti, A. Yonis, A. Harris, P. Mosaffa, Y. Fujita, A. Kabla, Y. Mao, B. Baum, J. J. Muñoz, M. Miodownik, and G. Charras, Nature Physics **15**, 839 (2019).
[57] O. Cochet-Escartin, J. Ranft, P. Silberzan, and P. Marcq, Biophysical Journal **106**, 65 (2014).
[58] P. P. Girard, E. A. Cavalcanti-Adam, R. Kemkemer, and J. P. Spatz, Soft Matter **3**, 307 (2007).
[59] L. Limat and J. Prost, Liquid Crystals **13**, 101 (1993).